Applications of Phase Diagrams and interpretation of microstructures

Lesley Cornish

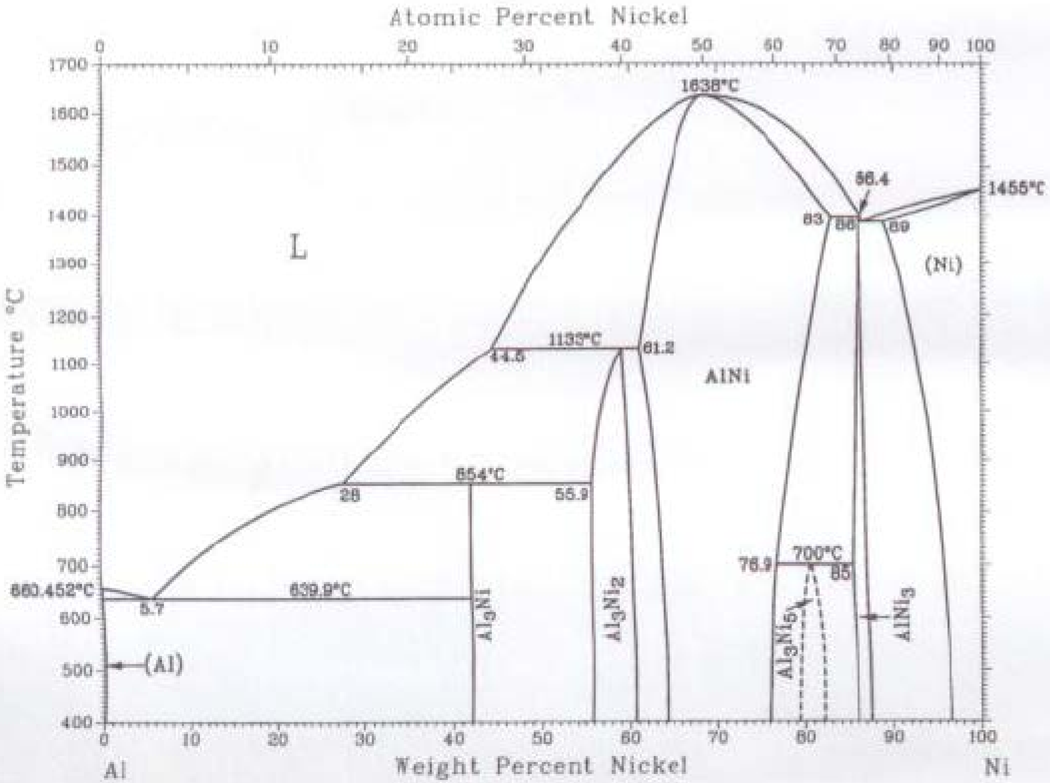
Atomic Percent Nickel
0
10
20
30
40
50
60
70
80
90
100
1700
1600
1500
1400
1300
1200
1100
1000
900
800
700
600
500
400
Temperature °C
1638°C
86.4
1455°C
83
86
89
L
(Ni)
1133°C
44.5
61.2
AlNi
854°C
28
55.9
76.9
700°C
85
660.452°C
639.9°C
5.7
Al_3Ni
Al_3Ni_2
Al_3Ni_5
$AlNi_3$
(Al)
0
10
20
30
40
50
60
70
80
90
100
Weight Percent Nickel
Al
Ni

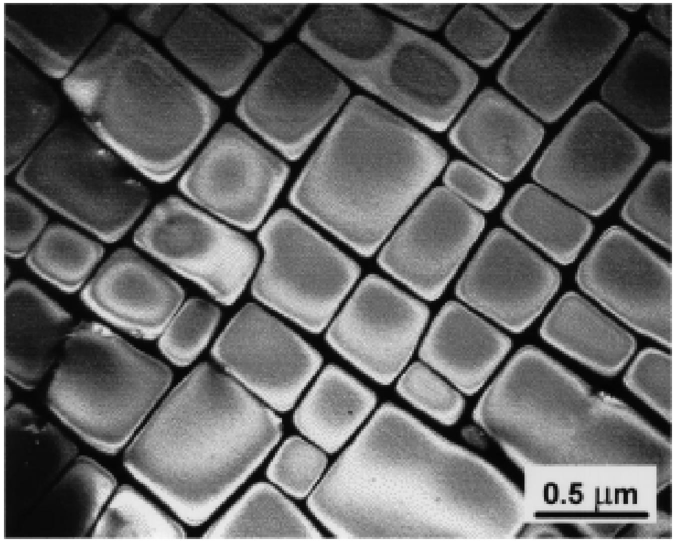
0.5 µm

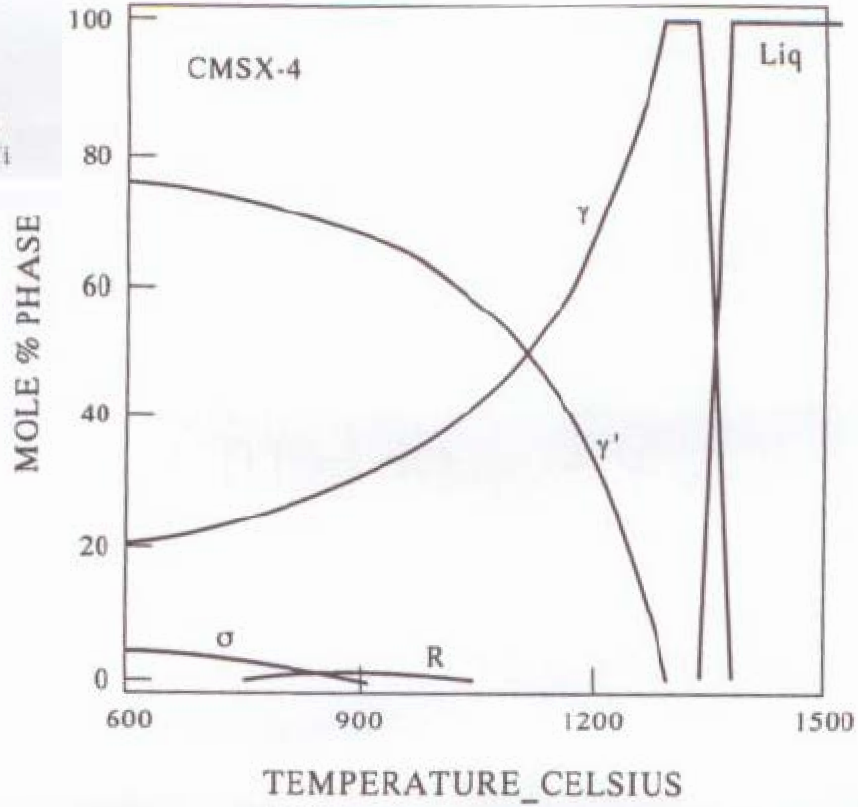
CMSX-4
Liq
100
80
60
40
20
0
MOLE % PHASE
γ
γ'
σ
R
600
900
1200
1500
TEMPERATURE_CELSIUS

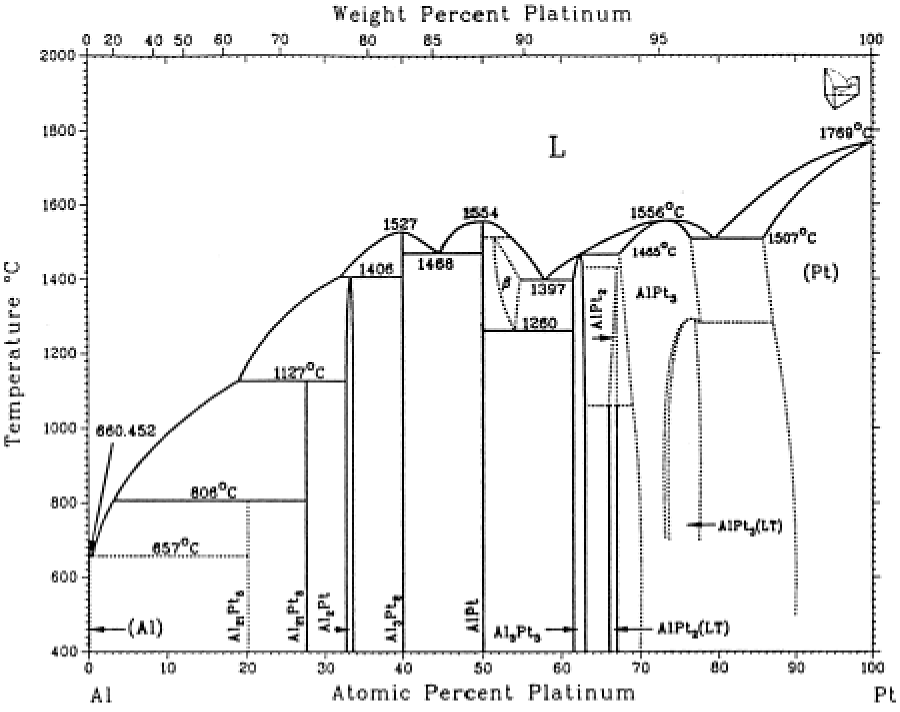

Fig. 1. Binary Pt–Al equilibrium phase diagram [11].

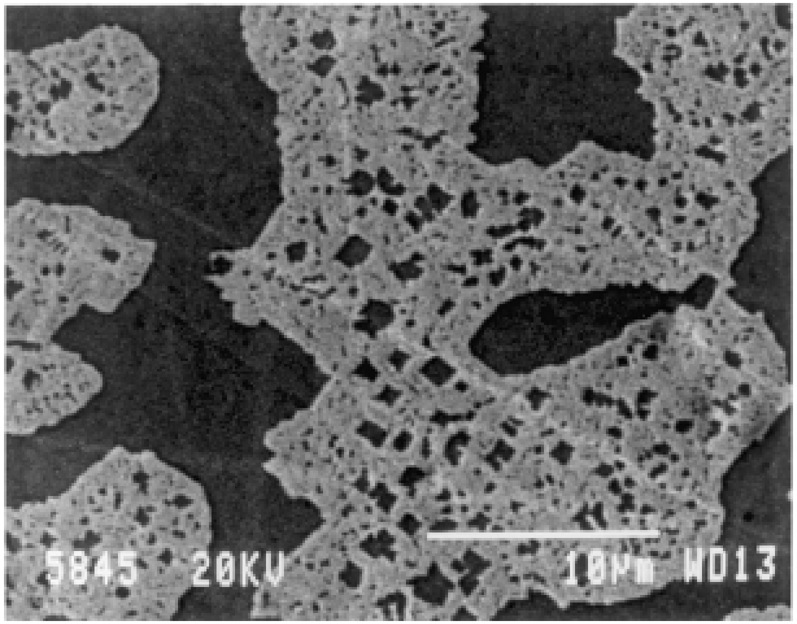

Fig. 11. SEM–BSE image showing the microstructure of the nominal Pt_{84}:Al_{14}:Cr_4 alloy.

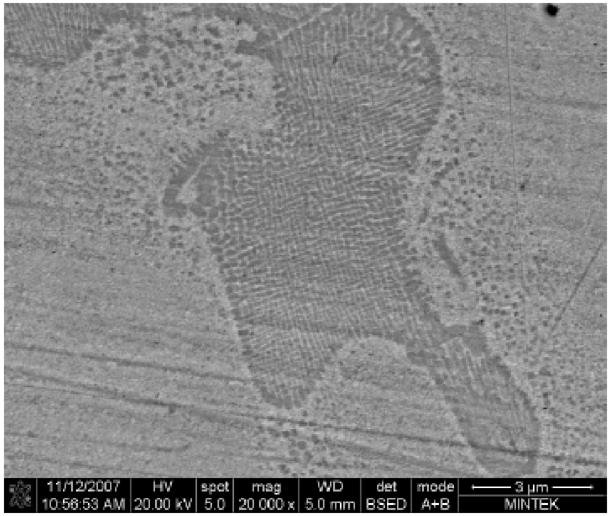

Figure 1. SEM-BSE image of nominal Pt_{82}:Al_{12}:Ru_2:Cr_4, showing the light (Pt) dendrites with darker ~Pt_3Al precipitates within, and the mainly dark eutectic/eutectoid of (Pt) + ~Pt_3Al.

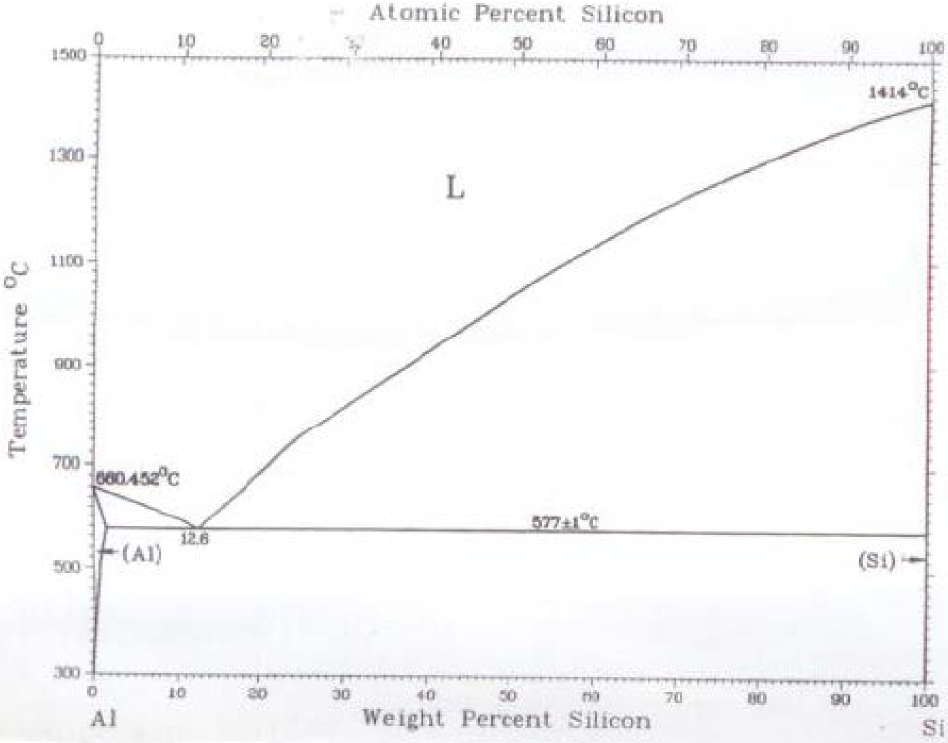

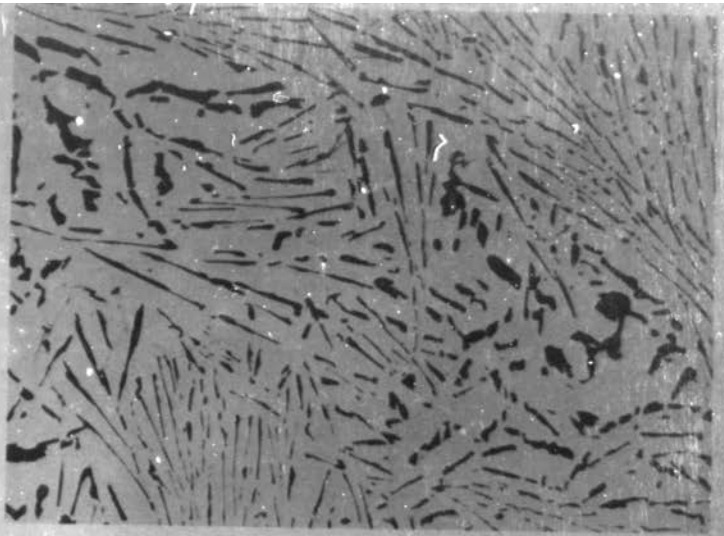

Fig. 17. Unmodified; this specimen from another batch of the alloy shows the variation possible in the silicon formation; it also contains approximately half the iron content of the preceeding specimens and it is difficult to detect the Al-Fe-Si phase. 250x.

(FM:F5)

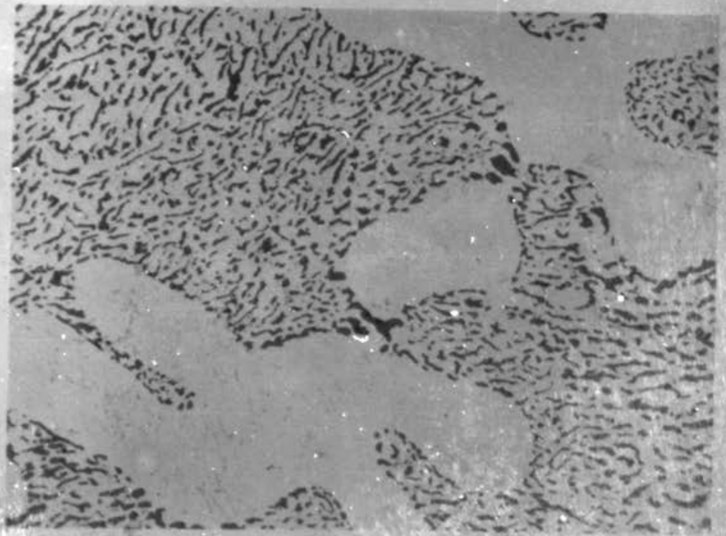

Fig. 18. Modified, the alloy corresponding in composition to that in Fig. 17, but again the magnification is higher. 300x.

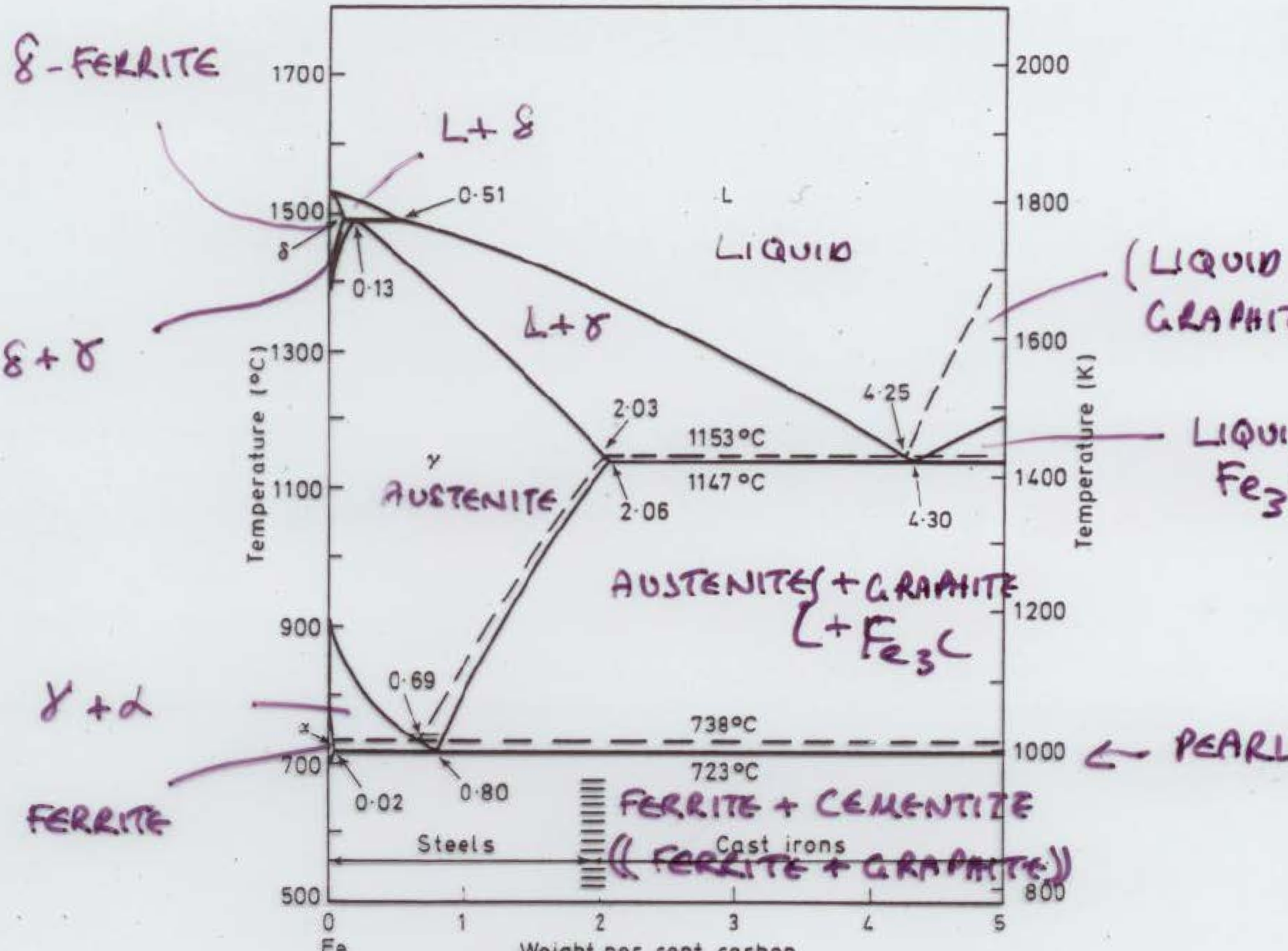
δ-FERRITE
L + δ
0·51
L
LIQUID
(LIQUID
GRAPHIT
δ
0·13
δ + γ
L + γ
4·25
2·03
1153 °C
1147 °C
LIQUI
Fe3
γ
AUSTENITE
2·06
4·30
AUSTENITES + GRAPHITE
(+ Fe3C
0·69
γ + α
α
738 °C
PEARL
723 °C
0·02
0·80
FERRITE
FERRITE + CEMENTITE
Steels
Cast irons
((FERRITE + GRAPHITE))
1700
1500
1300
1100
900
700
500
Temperature (°C)
2000
1800
1600
1400
1200
1000
800
Temperature (K)
0
1
2
3
4
5
Fe
Weight per cent carbon

Scanning electron micrograph of flake graphite in cast iron, showing the gross distortion and the interconnected nature of the graphite (x 5000) (Courtesy of M. G. Day, B.C.I.R.A.)

Cu-Zn

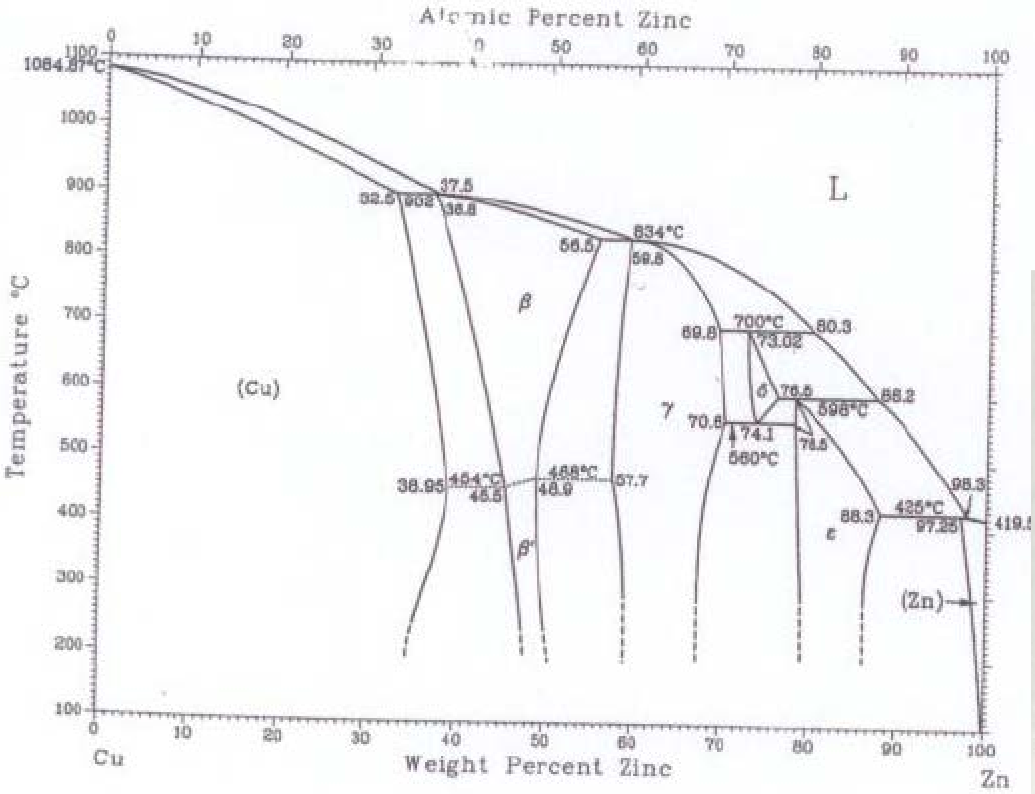

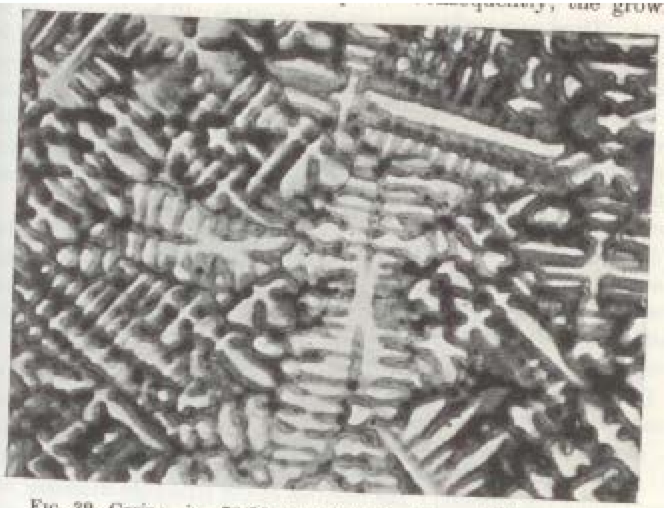

FIG. 39. Coring in 70/30 copper-zinc alloy, chill-cast. ×75. (It should be noted that the examples given in Figs. 38 (*b*), (*c*), 39 and 40 are terminal solid solutions.)

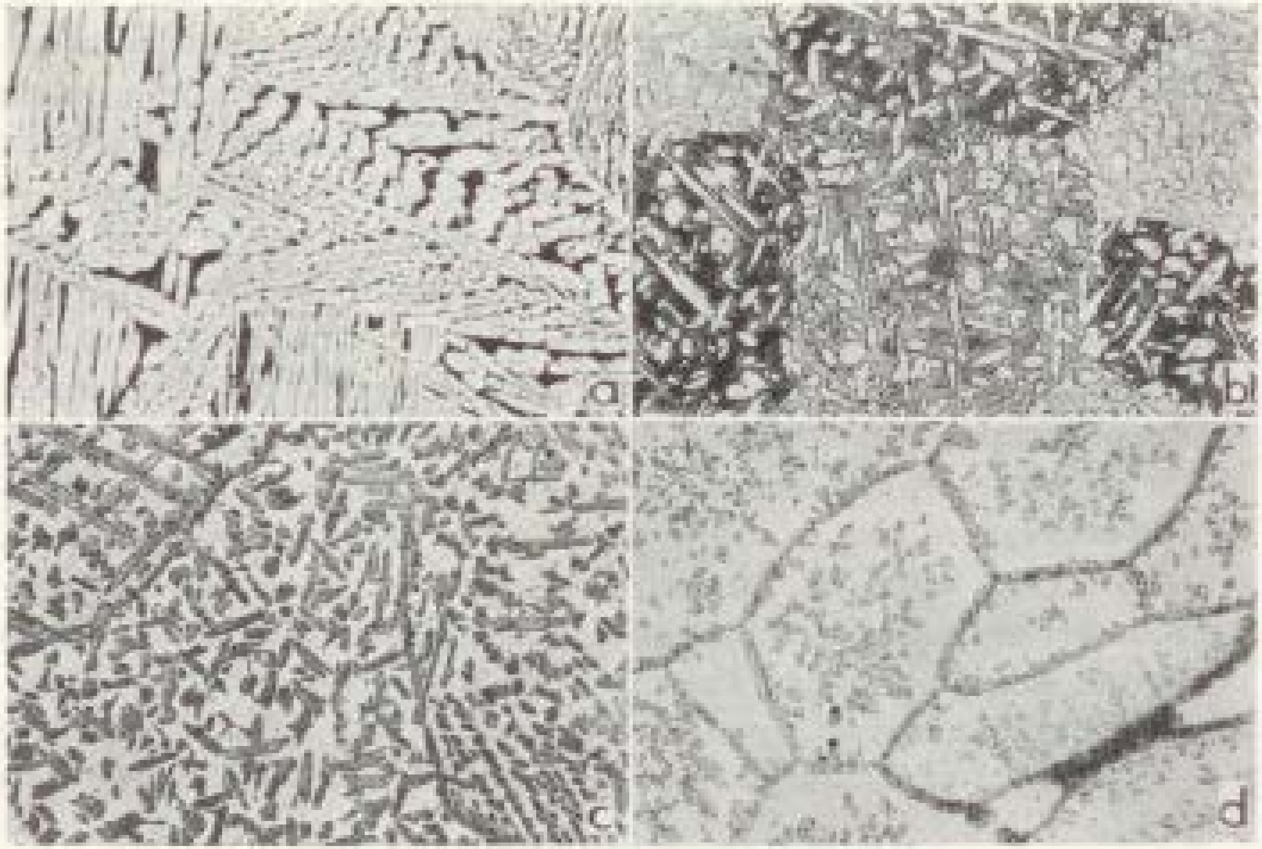

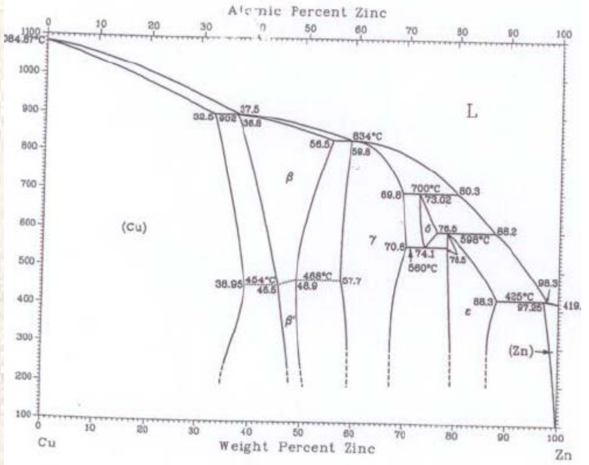

FIG. 62. Widmanstätten structures.

(*a*) Brass, cast (for phase diagram, see Fig. 392, p. 510). α (light) precipitated in β (dark), etched in alcoholic ferric chloride. × 30.

(*b*) Similar material but containing less α and showing clearly the varying orientation of the β grains. × 50.

(*c*) α-β brass, but showing reversal of etching by ammonium persulphate. × 50.

(*d*) Brass, cast: γ-phase precipitated in β. × 50.

(*e*) Copper-4 per cent beryllium (phase diagram, Fig. 384, p. 503). Quenched from molten condition in water: incipient or arrested precipitation of α in metastable β. × 700.

Old solder! Choose composition for flowability: eutectic

pastiness (to bend joint): off eutectic

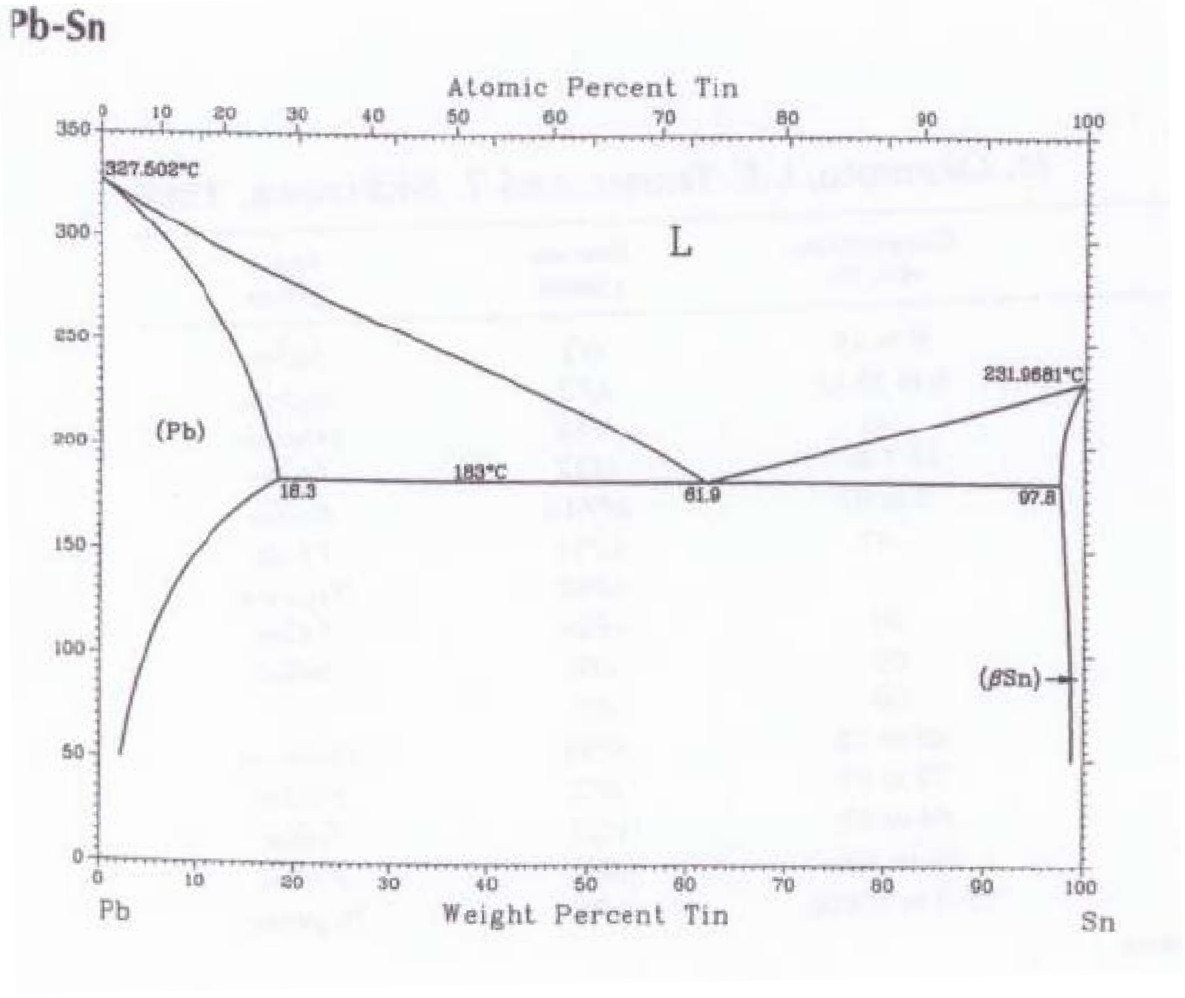

WC-Co hardmetals

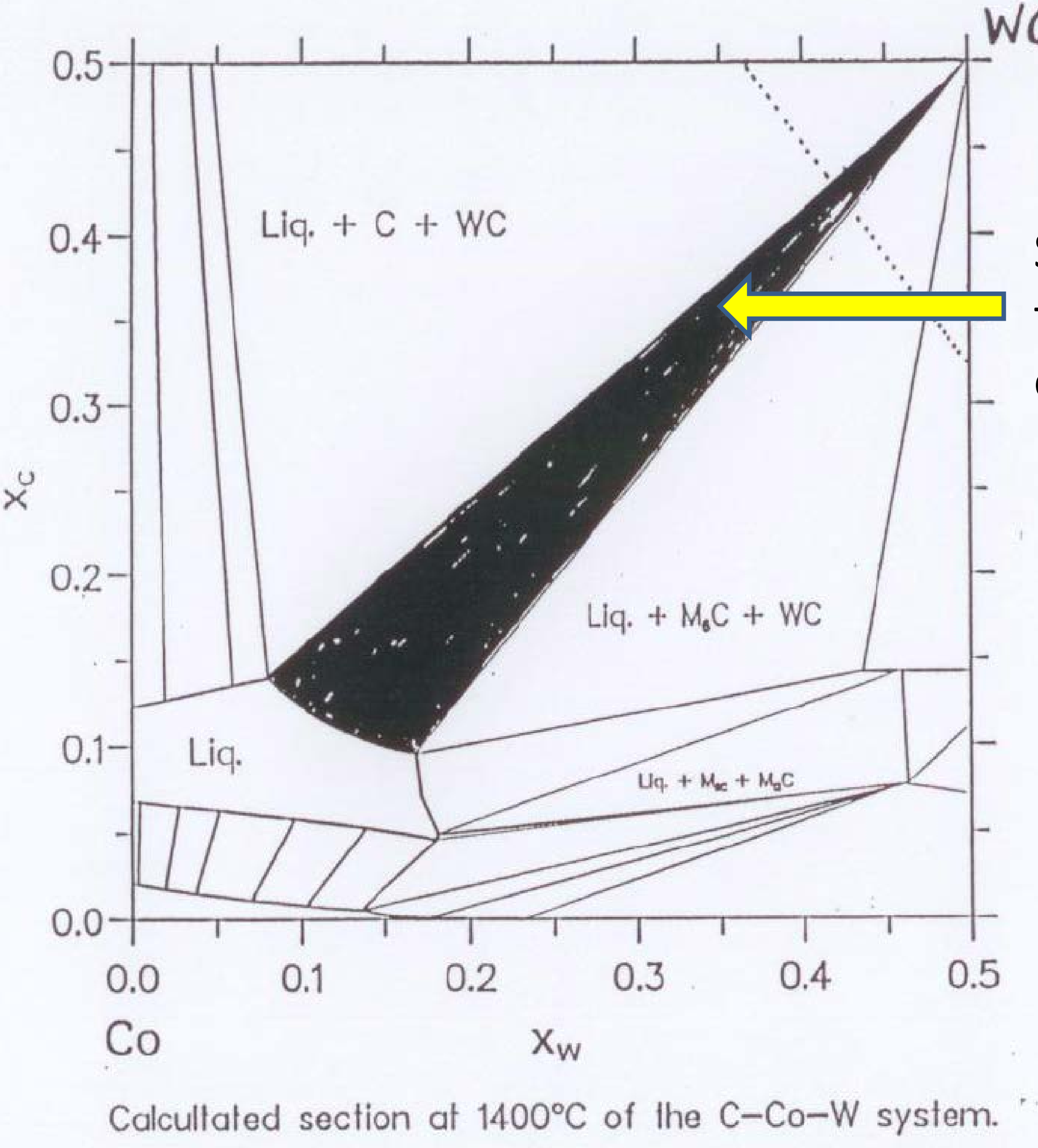

Calcultated section at 1400°C of the C–Co–W system.

Sintering region to avoid graphite or sigma

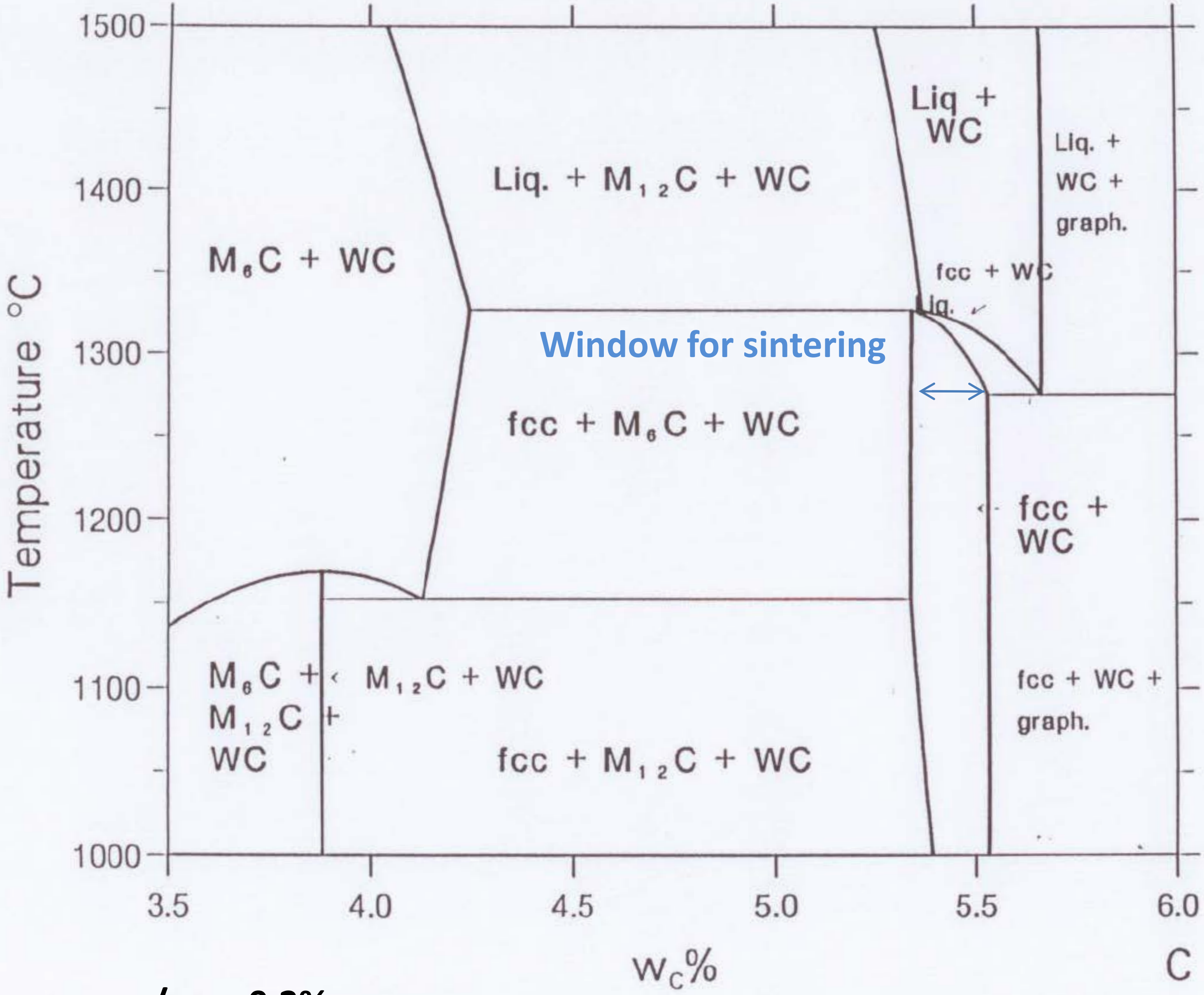

Window for sintering

x_{Co}/x_W = 0.2%

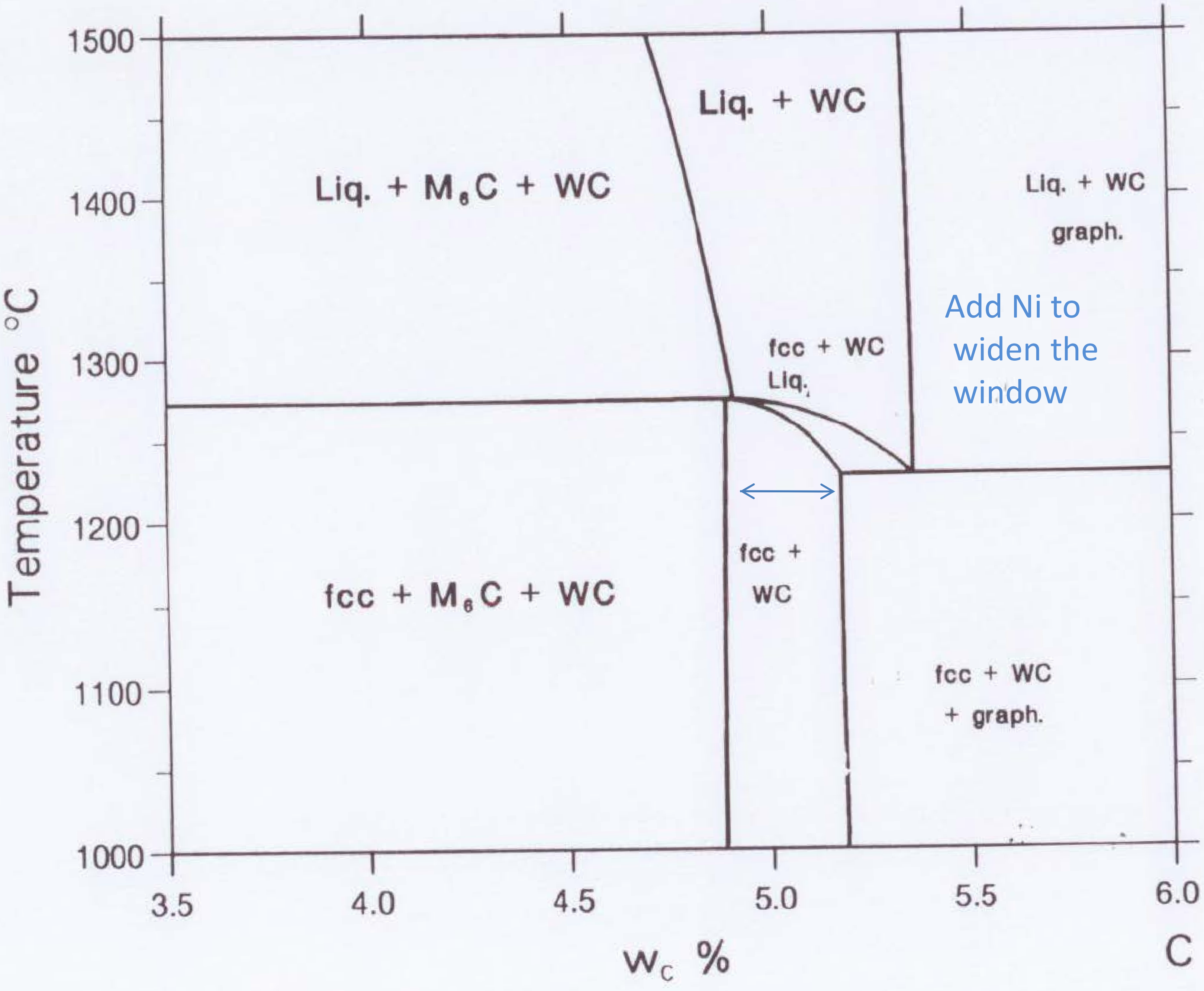

Add Ni to widen the window

To remove undesirable magnetic ferrite

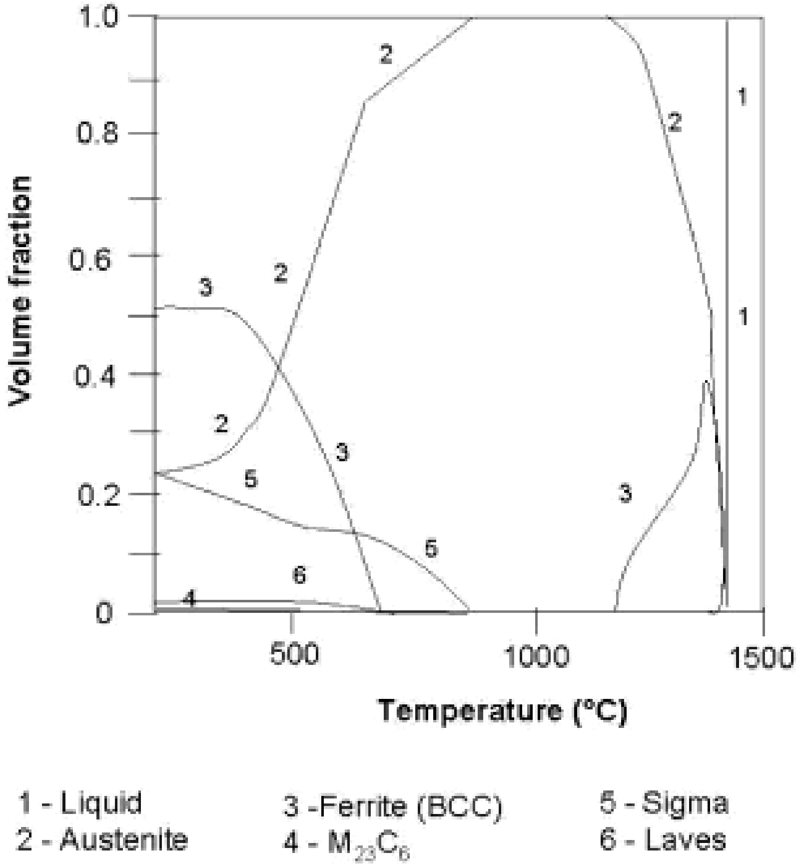

Fig. 1. Thermo-Calc™ predicted multi-component diagram of 0 PERSS.

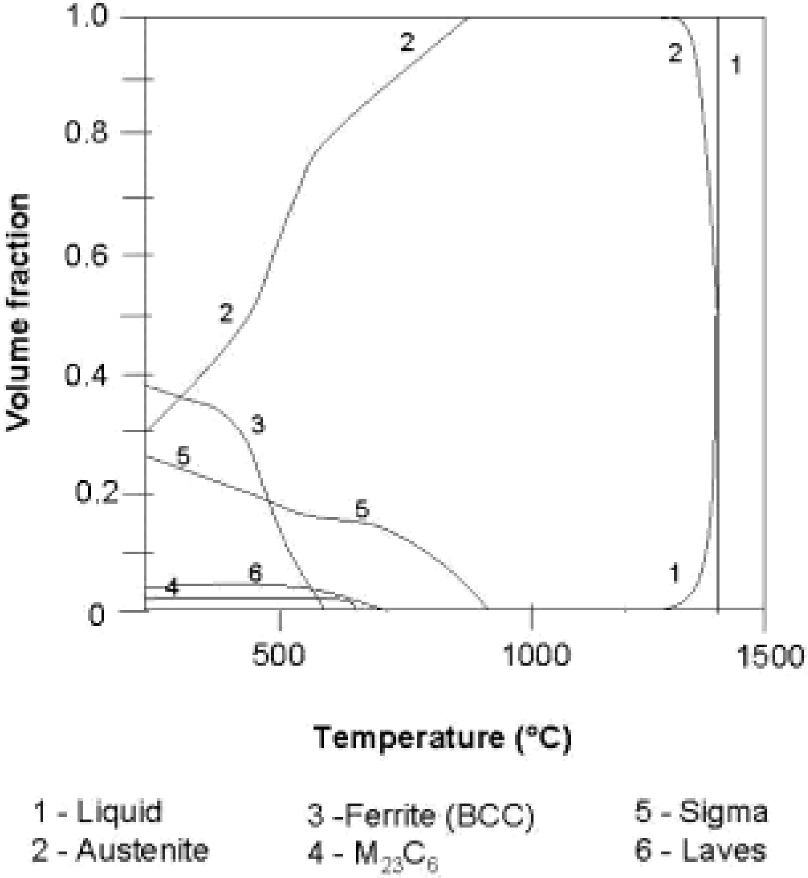

Fig. 2. Thermo-Calc™ predicted multi-component diagram of 10 PERSS.

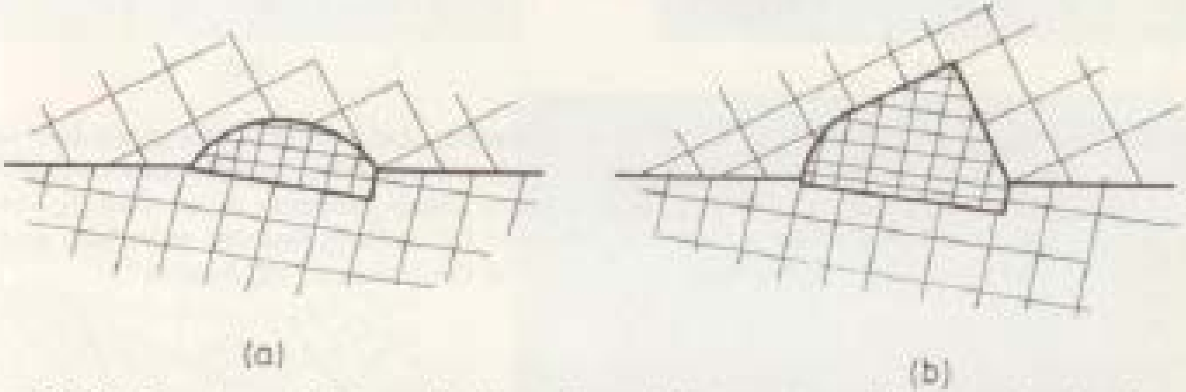
(a) (b)

Figure 6.16 Drawings of the nucleation of precipitates at a grain boundary for the cases of (a) coherent and incoherent interfaces, and (b) coherent and semi-coherent interfaces

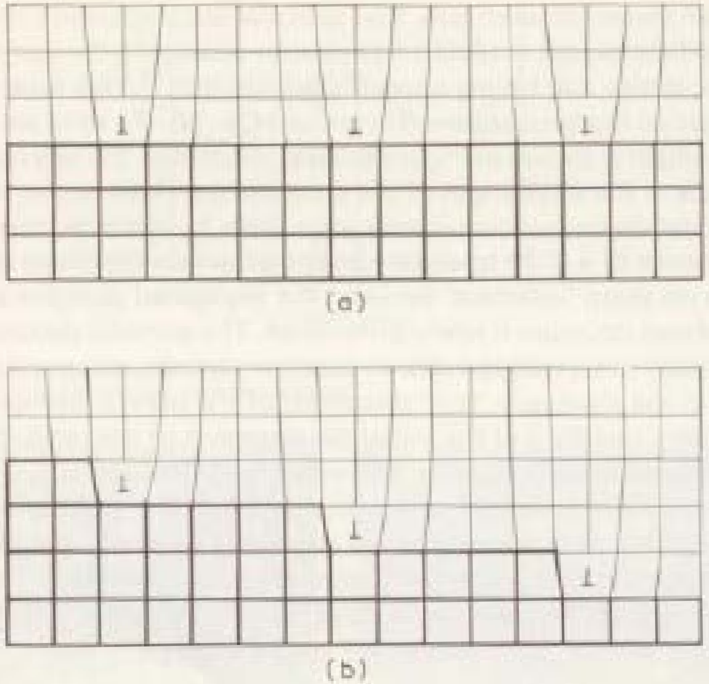

(a)

(b)

Possible interfacial structures of semi-coherent interfaces for (a) planar interfaces, (b) stepped interfaces

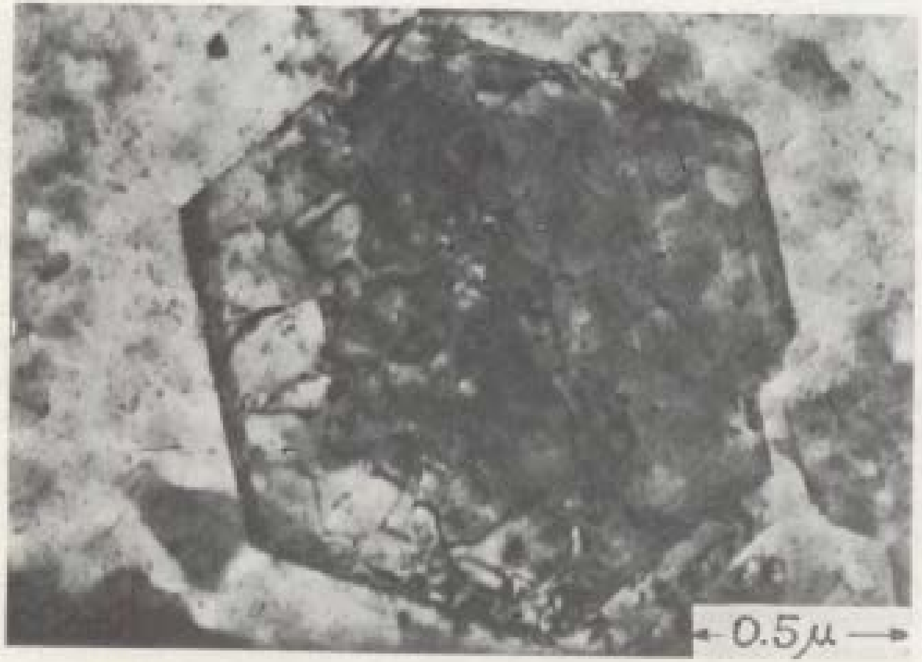

Figure 6.37 Interfacial dislocations on the broad faces of a γ-phase precipitate in an Al–Ag alloy. (Courtesy of C. Laird[17])

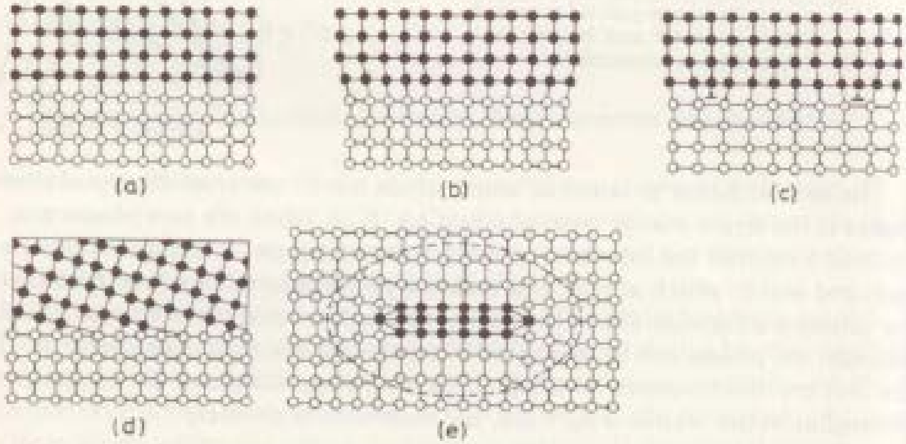

Figure 6.8 Schematic drawings of the atomic arrangements at interfaces for different values of the misfit parameter, δ: (a) perfectly coherent; (b) elastically strained, coherent; (c) semi–coherent; (d) incoherent; (e) this drawing shows the strain around a precipitate caused by a difference in lattice spacing normal to the broad faces of the precipitate, such as is found during the precipitation of θ″ from Al–Cu alloys

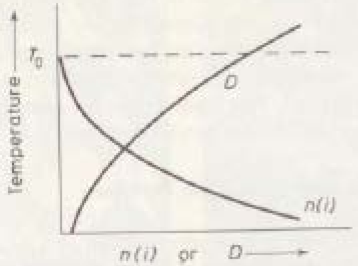

Temperature dependence of the frequency of cluster formation, n(i), and the diffusion coefficient, D

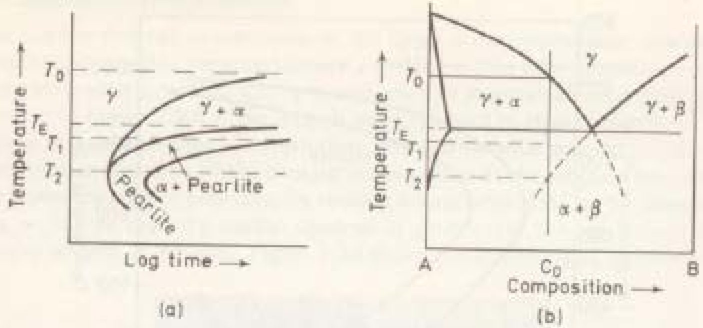

Figure 7.30 (a) TTT curve of a hypo-eutectoid alloy. (b) Equilibrium diagram and temperature range T_E to T_1 over which pro-eutectoid ferrite is present in isothermally decomposed alloys

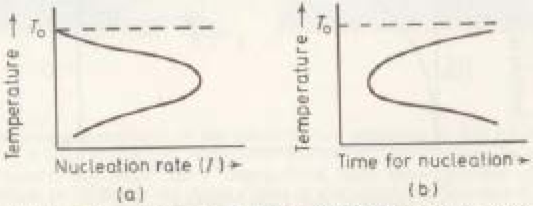

(a) Rate of nucleation, I, as a function of temperature. (b) Time required for initiation of nucleation as a function of temperature

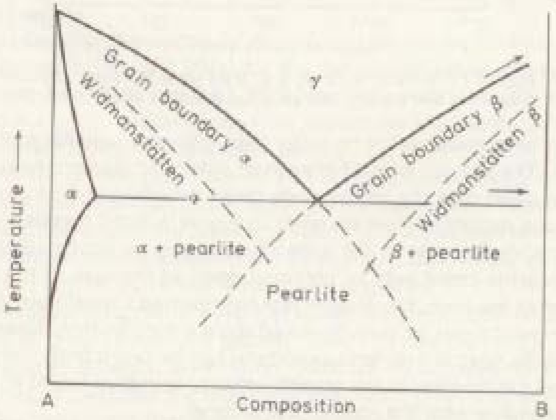

Equilibrium diagram showing ranges of temperature and composition over which the various reaction products appear during isothermal decomposition

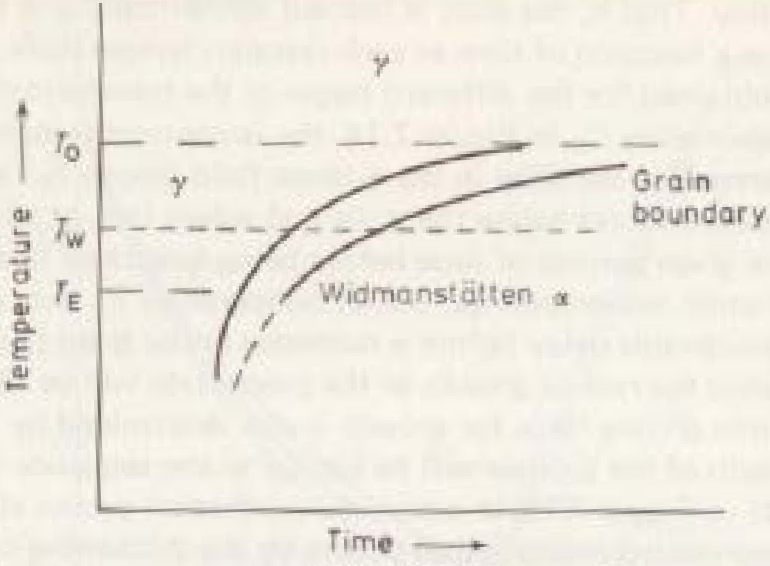

Figure 7.17 *Typical TTT curve of α deposition from γ, and showing the temperature ranges over which grain boundary networks and Widmanstätten morphologies arise*

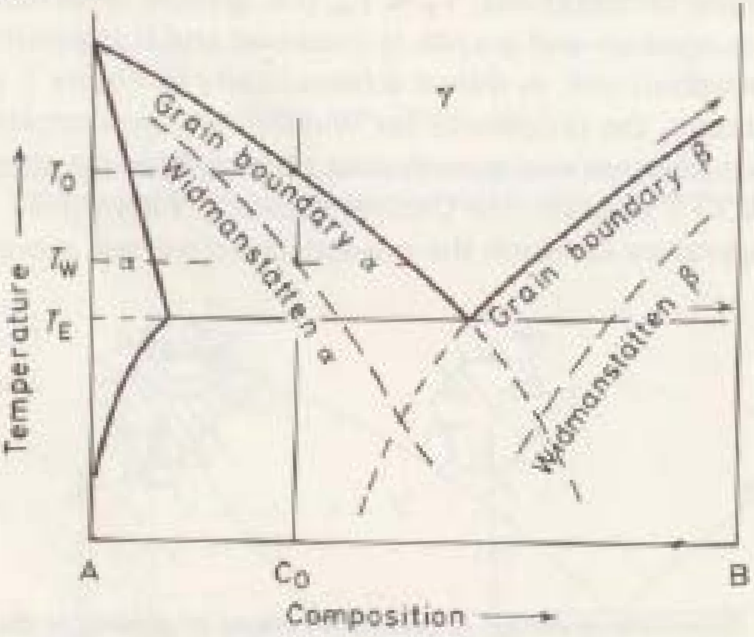

Figure 7.18 *Superpositioning of the morphology ranges obtained from curves like Figure 7.17 on to the equilibrium diagram*

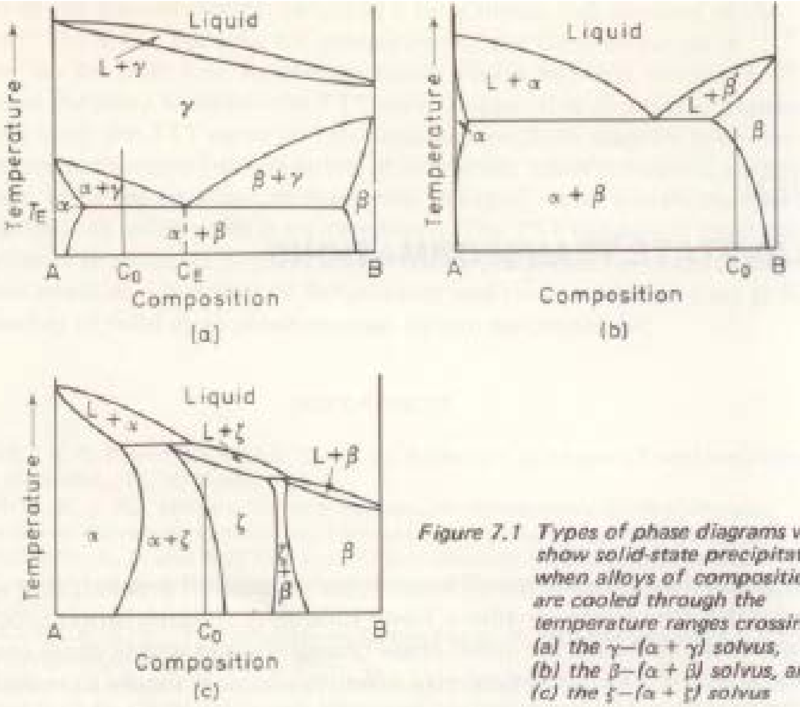

Figure 7.1 Types of phase diagrams which show solid-state precipitation when alloys of composition C_0 are cooled through the temperature ranges crossing (a) the γ–(α + γ) solvus, (b) the β–(α + β) solvus, and (c) the ζ–(α + ζ) solvus

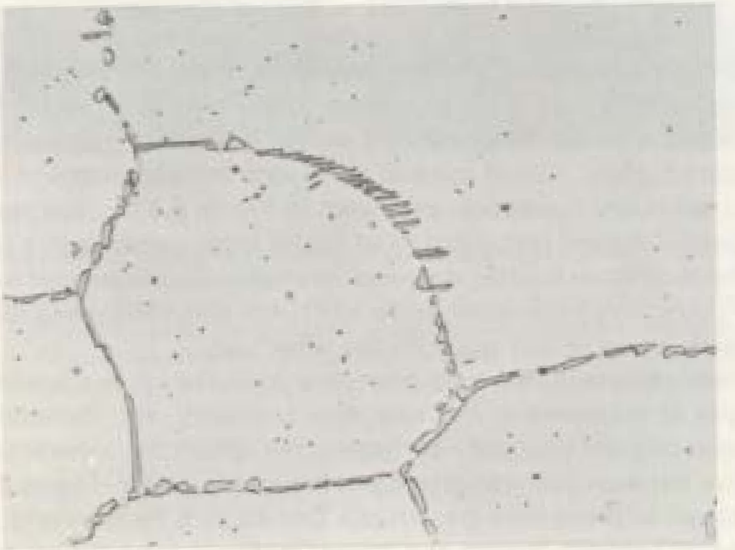

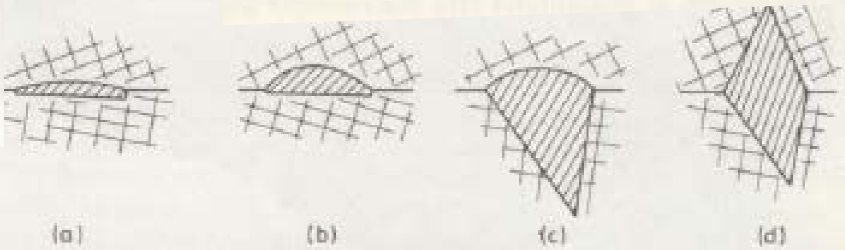

Figure 7.2 Nucleation and growth sequence of a precipitate at a grain boundary. (a) the nucleation event generally occurs with the production of one semi-coherent interface and one incoherent interface on opposite sides of the nucleus; (b) growth at low supersaturations favours the propagation of the incoherent interface; (c) growth at high supersaturations leads to the migration of the semi-coherent interface; (d) if certain crystallographic conditions are satisfied, semi-coherent interfaces can develop on both sides of the precipitate

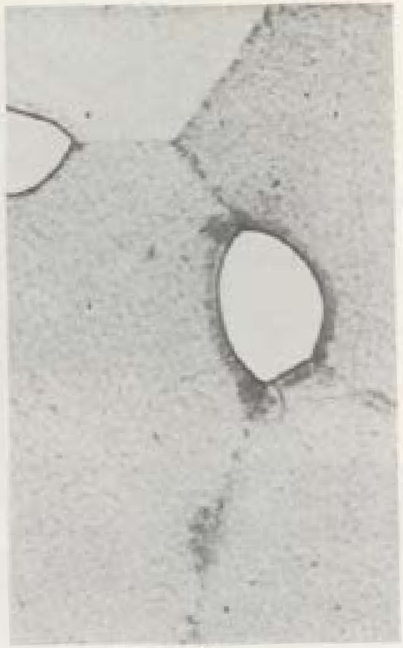

(b)

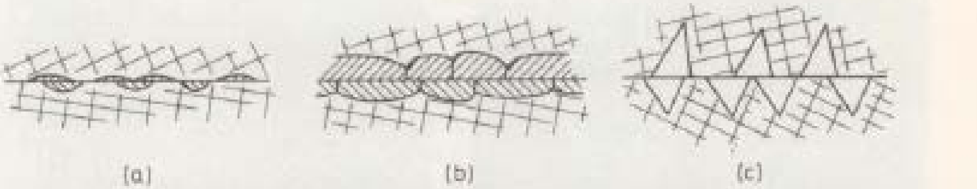

Figure 7.3 Nucleation and growth of multiple precipitates at a grain boundary. (a) The semi-coherent and incoherent interfaces of the individual precipitates are arranged randomly along the boundary plane; (b) at low supersaturations the incoherent boundaries overgrow the semi-coherent boundaries, giving rise to a grain boundary network of precipitate; (c) at high supersaturations the semi-coherent interfaces develop

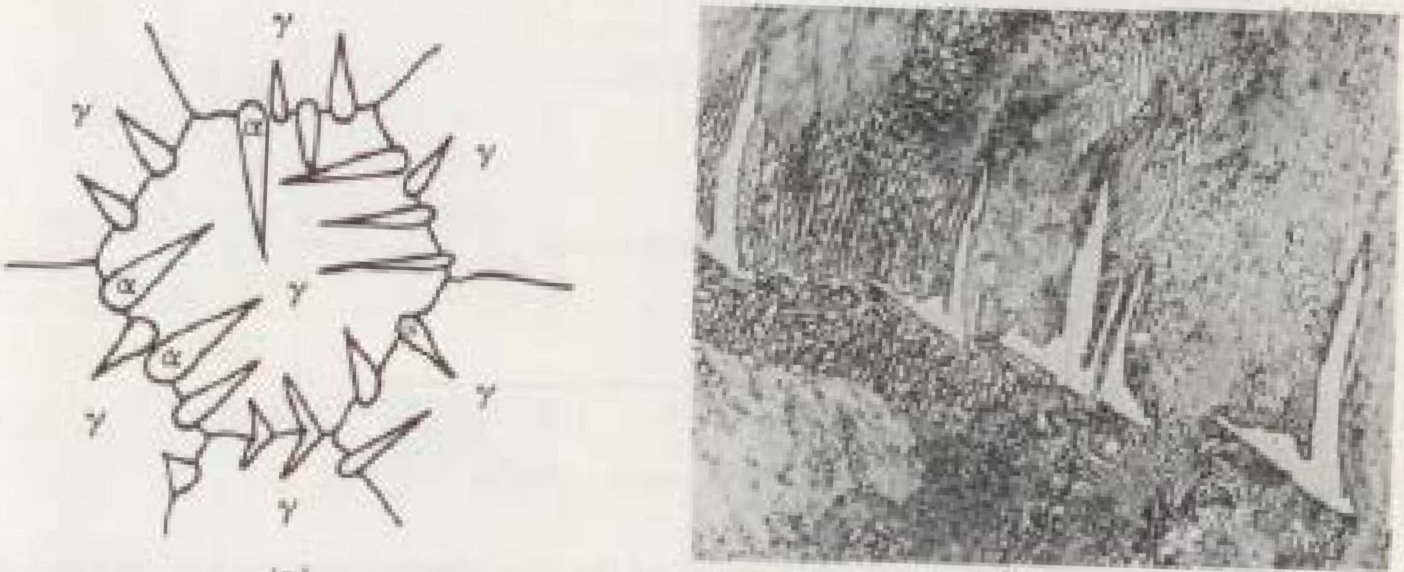

(a) (b)

Figure 7.10 (a) Schematic drawing of Widmanstätten growth of α in γ. (b) Micrograph of a hypoeutectoid Cu–11 wt % Al (23 at % Al) alloy moderately air-cooled from 1050 K (777°C) (× 350)

(a) (b) (c)

Figure 7.16 Schematic drawings of successive stages of growth in the isothermal decomposition of γ to produce a Widmanstätten morphology of α

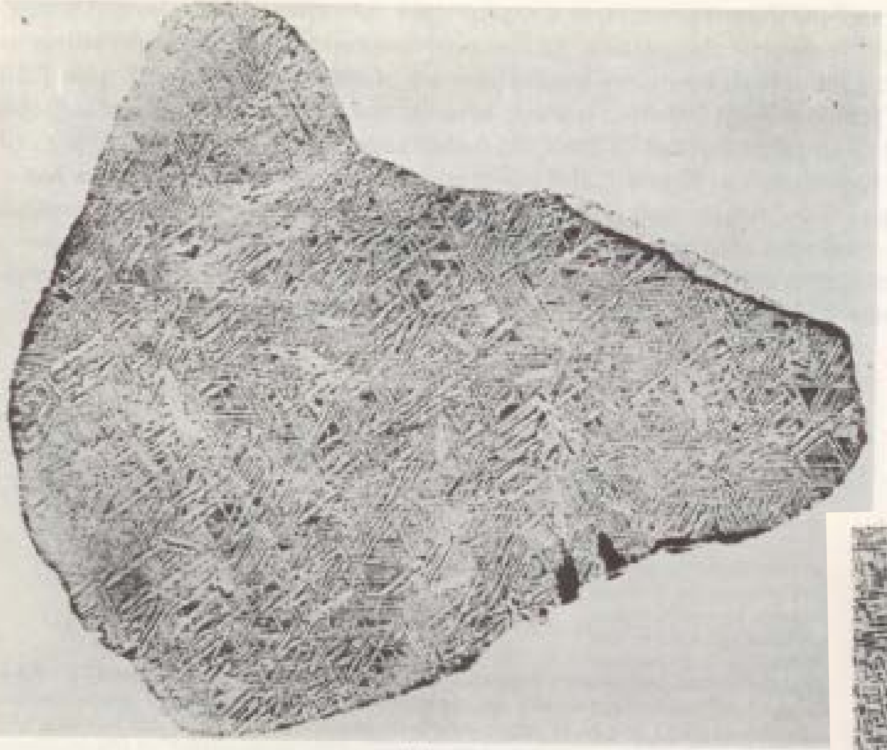

(a)

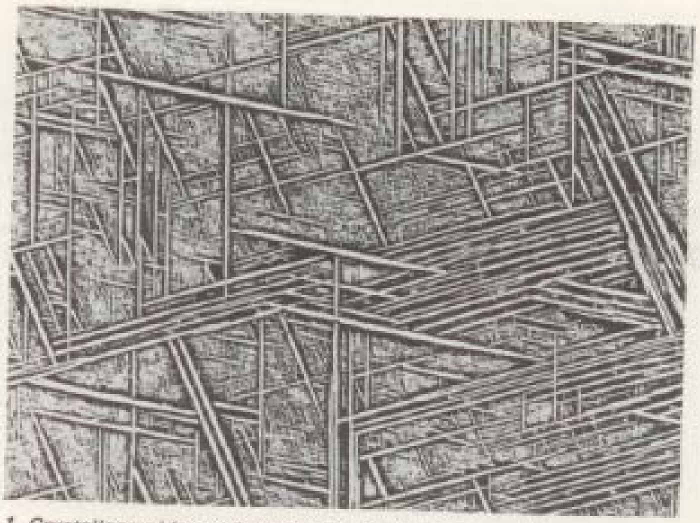

Figure 6.1 Crystallographic precipitation of Ag_3Al compound from a supersaturated Al–Ag solid solution. This type of morphology is known as Widmanstätten (× 200)

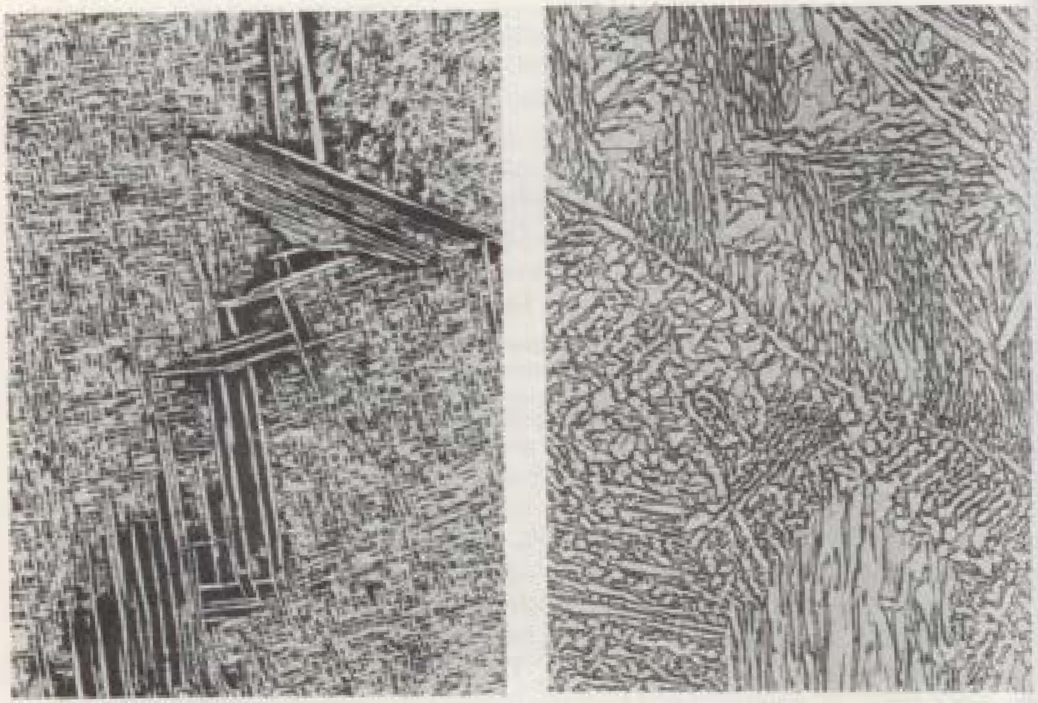

(b) (c)

Figure 7.4 Typical Widmanstatten morphologies. (a) Copy of the original ink-print taken by Aloys von Widmanstätten of the Elbogen meteorite (× 0·5); (b) Al–8 at % Ag alloy showing Widmanstätten precipitation of the Ag_3Al phase (× 400). Note the largeness of the precipitates in the boundary compared with the matrix precipitates; (c) rods of α-brass precipitated from β-brass (× 400)

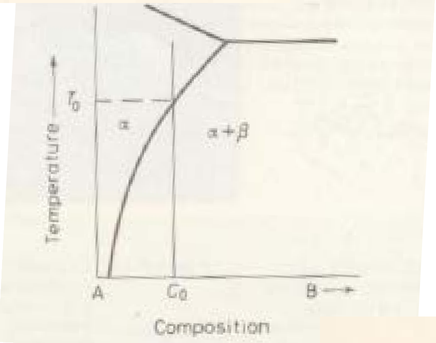

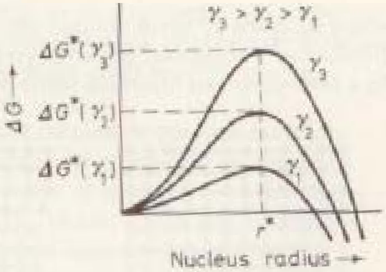

Figure 6.6 *The free energy barrier to nucleation drawn schematically as a function of interfacial energy between the precipitate and matrix, γ_1, γ_2 and γ_3 representing the interfacial energies of coherent, semi-coherent and incoherent boundaries, respectively*

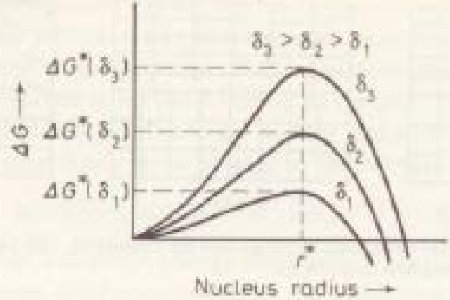

Figure 6.7 *The free energy barrier to nucleation drawn schematically as a function of the misfit parameter δ at the precipitate-matrix interface*

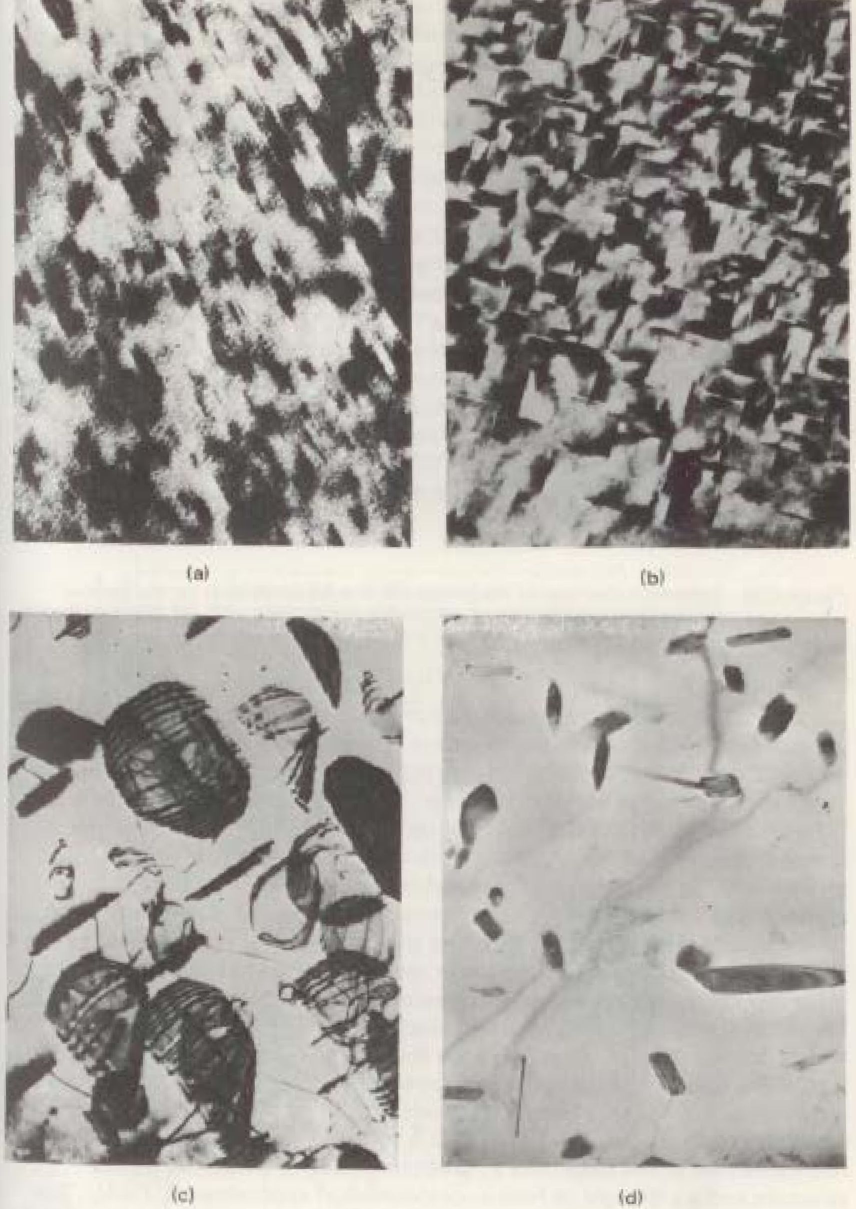

Figure 6.25 *Electron micrographs of the precipitation sequence in Al–1·7 at.% Cu (Al–4 wt.% Cu) alloys. (a) Guinier–Preston zones evident by strain contrast effects (× 300 000); (b) θ'' precipitates, again showing strain contrast effects (× 70 000); (c) dislocations at the interfaces between θ' and Al (× 20 000); (d) incoherent particles of equilibrium θ in the Al matrix [(a) and (b) Courtesy of R. B. Nicholson.[3] (c) Courtesy of G. C. Weatherly. (d) Courtesy of C. Laird]*

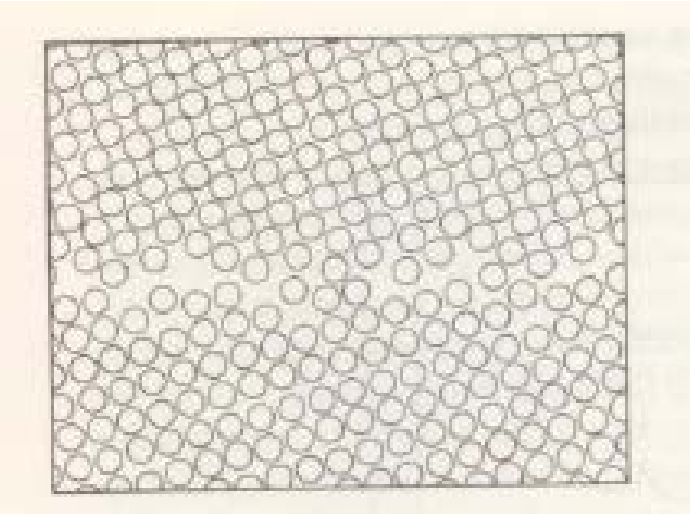

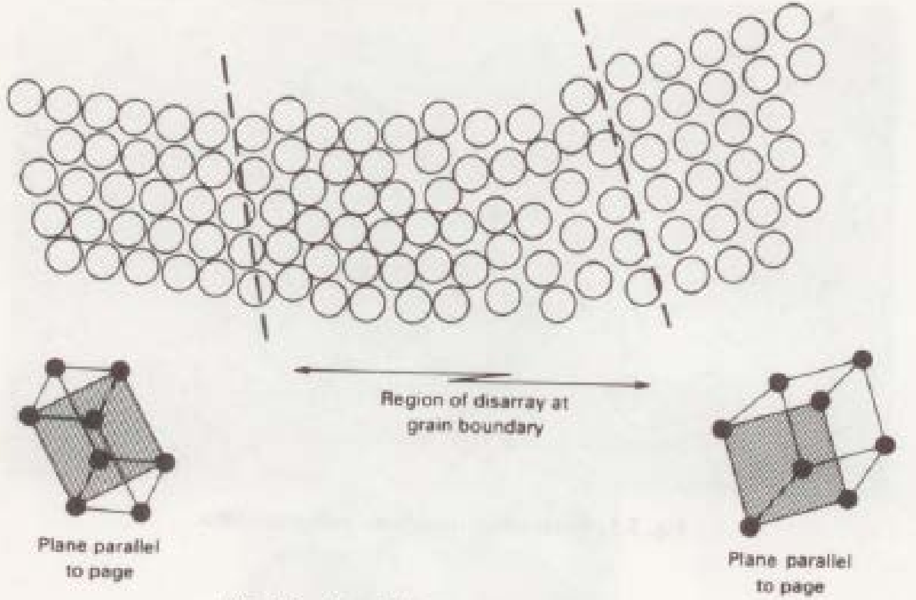

Fig. 3.5. Atomic disarray at grain boundary.

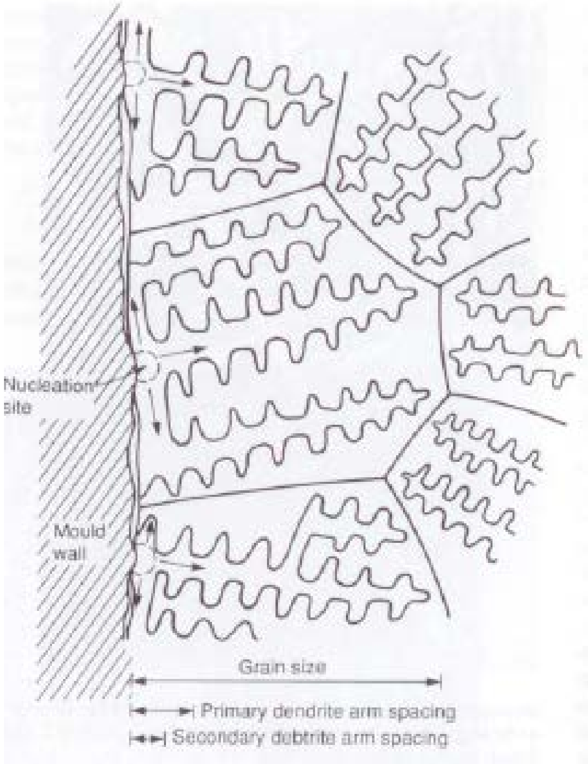

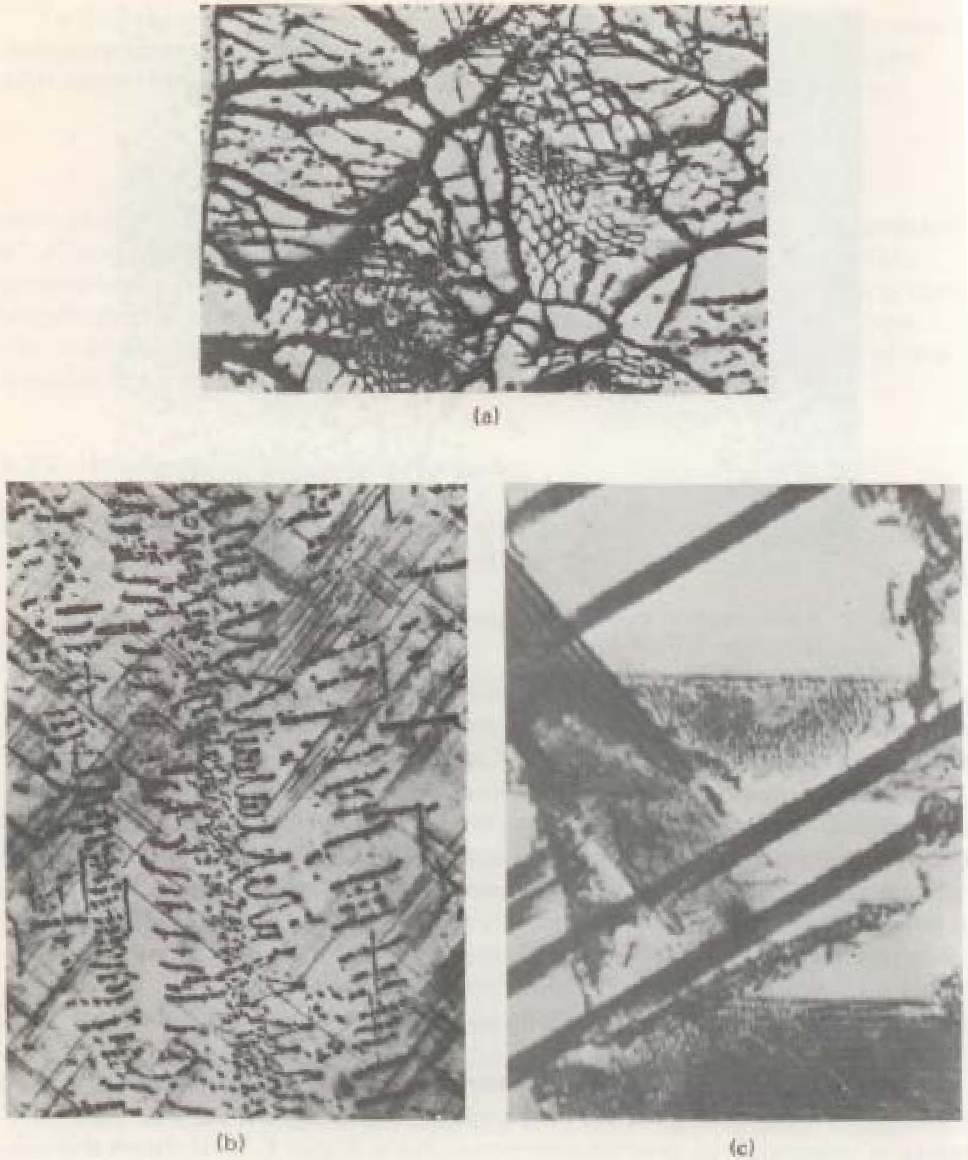

(a)

(b)

(c)

Figure 6.14 *Examples of precipitate nucleation on dislocations. (a) Particles of silver precipitated along dislocation lines in silver bromide (× 1000). (b) Precipitation on helical dislocations in an* Al–2·7 wt.% Cu–1·36 Mg *alloy (× 14 000). (c) Niobium nitride precipitation at dislocation stacking faults in an* Fe–Ni–Cr–Nb *alloy (× 75000). [(a) Courtesy of J. W. Mitchell*[6]*. (b) Courtesy of G. E. Weatherly*[7]*. (c) Courtesy of R. W. K. Honeycombe]*

Figure 6.13 Precipitate free zone around a grain boundary in an Al–Ge alloy (× 20 000) (Courtesy of G. W. Lorimer[4])

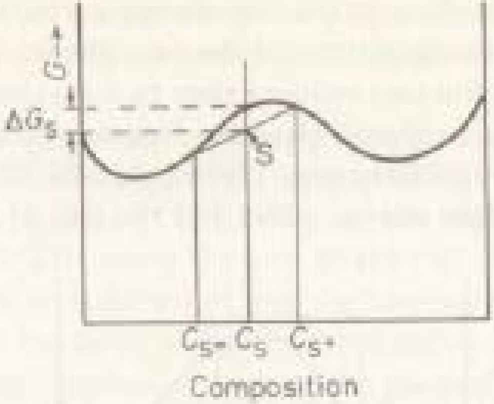

Figure 6.34 *Schematic drawing showing the decrease in free energy of an alloy undergoing spinodal decomposition*

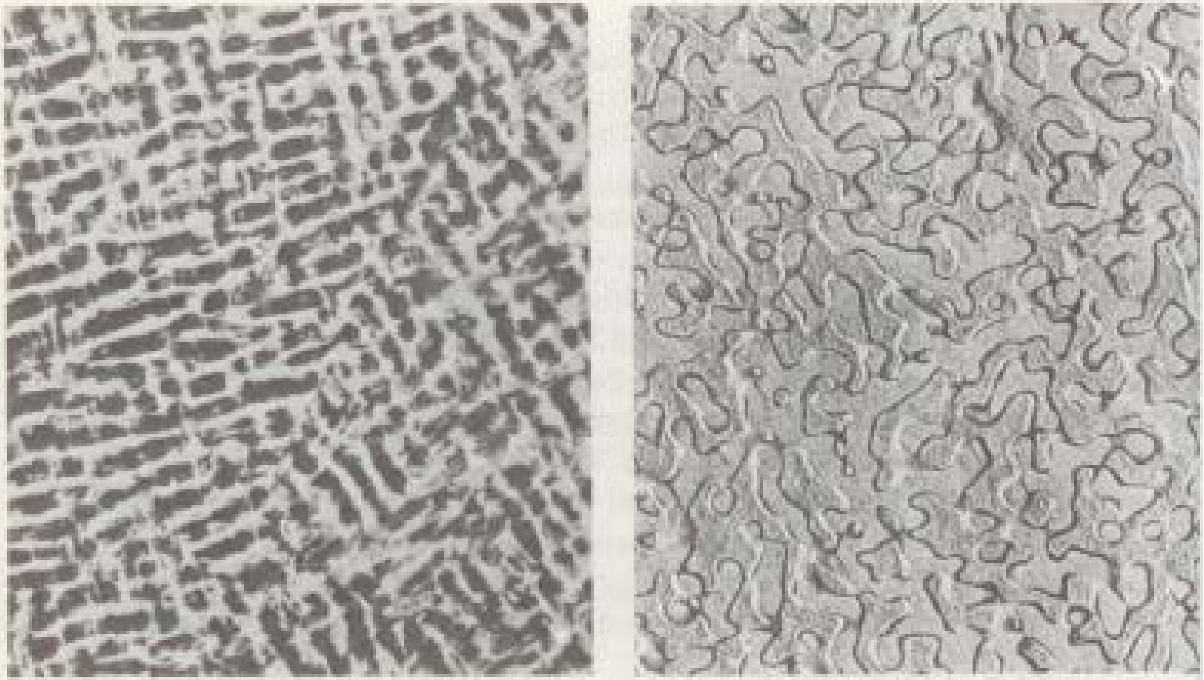
(a)

(b)

Figure 6.35 *Examples of spinodally decomposed materials. (a)* Cu—Ni—Fe alloy *(x 80 000). (b) Sodium borate glass (x 100 000) [(a) Courtesy of R. B. Nicholson.*[15] *(b) Courtesy of R. J. Charles*[16]*]*